Soft Matter

Accepted Manuscript

Hydrogen Bonding Strength of Diblock Copolymers Affects the Self-Assembled Structures with Octa-Functionalized Phenol POSS Nanoparticles

Yi-Syuan Lu, Chia-Yu Yu, Yung-Chih Lin, and Shiao-Wei Kuo*

In this study, the influence of functional groups by the diblock copolymers of poly(styrene-*b*-4-vinylpyridine) (PS-*b*-P4VP), poly(styrene-*b*-2-vinylpyridine) (PS-*b*-P2VP), and poly(styrene-*b*-methyl methacrylate) (PS-*b*-PMMA) on their blends with octa-functionalized phenol polyhedral oligomeric silsesquioxane (OP-POSS) nanoparticles (NPs) were investigated. The relative hydrogen
10 bonding strengths in these blends follow the order of PS-*b*-P4VP/OP-POSS > PS-*b*-P2VP/OP-POSS > PS-*b*-PMMA/OP-POSS based on Kwei equation from differential scanning calorimetry (DSC) and Fourier transform infrared spectroscopy analyses. Small-angle X-ray scattering and transmission electron microscopy analyses show the morphologies of the self-assembly structures strongly dependent on the hydrogen bonding strength at relatively higher OP-POSS content. The PS-*b*-P4VP/OP-POSS hybrid complex system with the strongest hydrogen bonds shows the order–order transition from lamellae to cylinders and finally to body-centered-cubic spheres upon
15 increasing OP-POSS contents. However, PS-*b*-P2VP/OP-POSS and PS-*b*-PMMA/OP-POSS hybrid complex systems having relatively weaker hydrogen bonds, transformed from lamellae to cylinder structures at lower OP-POSS contents (<50 wt%), but formed disordered structures at relative high OP-POSS contents (> 50 wt%).

Introduction

20 Self-assembled structure from diblock copolymers (BCPs) including alternative lamellae, bicontinuous gyroids, hexagonally packed cylinders, and spheres and organic/inorganic hybrid materials constitute a new fascinating field in polymer science.[1,2] Many progresses have been widely in fundamental understanding
25 of organic/inorganic hybrid systems formed from inorganic nanoparticles and block copolymers, the properties of which cannot be replicated in organic/organic block copolymers,[3–5] such as poly(styrene-*b*-dimethylsiloxane),[6,7] and poly(methyl methacrylate–*b*–methacryloyl polyhedral oligomeric
30 silsesquioxane) diblock copolymers.[8-10] Polyhedral oligomeric silsesquioxane (POSS) with unique cage-like structure with ca. 1-3 nm nanoscale dimension as nanoparticles (NPs), often used for organic/inorganic hybrid materials.[11–14]

In addition to the preparation of organic/inorganic block
35 copolymers, blending of inorganic nanoparticles within organic/organic diblock copolymers to form BCP/NP composites is quite interesting because of their possible applications in sensors, photonics, and nanodevices.[15–21] The self-assembled structure from diblock copolymers are strongly dependent on the
40 degree of polymerizations (N), interaction parameters (χ), and the volume fractions (f) of the diblock copolymer segments.[2] At low values of χN, the diblock copolymer is usually phase-mixed. The possible disorder-to-order transition (DOT) may occur when χN increases. Therefore, the dispersion of nanoparticles in diblock
45 copolymer is relation with the increasing enthalpy change from the creation of polymer-NP interfaces and the decreasing in polymer conformational entropy.[22–25]

Generally, using compatible or miscible ligands with one of the block segments can provide the preferential segregation of
50 NPs within the compatible or miscible block segment. For instance, the use of polystyrene (PS) or poly(2-vinylpyridine)

Department of Materials and Optoelectronic Science, Center for Nanoscience and Nanotechnology, National Sun Yat-Sen
55 University, Kaohsiung, 804, Taiwan.
E-mail: kuosw@faculty.nsysu.edu.tw

95

(P2VP) homopolymer as ligand for the Au nanoparticle can mediate the distribution of Au nanoparticle in the self-assembled
60 structure of PS-*b*-P2VP block copolymers[26–30] Since the ligand of NPs is chemical identical or similar to one of block segments, the enthalpically neutral NPs lead the entropic penalty and thus provide the self-assembly structure to disorder morphology at relative higher NPs contents. To solve the disorder morphology
65 problem, using strong hydrogen bonding has been widely studied for blending block copolymers with nanoparticles, significantly improving miscibility behavior or the swelling diblock copolymer segments without macro-phase separation and order–order morphological transition.[15–21] For example, several nanoparticles
70 such as CdS, Au, and POSS modified on their surfaces with hydroxyl or multiple hydrogen bonding functional groups are able to interact with the poly(ethylene oxide) (PEO), P4VP, and poly(vinylbenzyl thymine) (PVBT) domains of diblock copolymers. This strong intermolecular hydrogen bonds can
75 significantly decrease the macrophase separation possibility of the nanoparticles and then in favor of microphase separation.[33–40] For example, we have investigated the ligand effects of POSS nanoparticle, where one is chemical similar to PS block segment and the other has the hydrogen bonding interaction with P4VP
80 block segmentin our previous study.[41] The relative weaker hydrophobic interaction between the aromatic group of the PS block segment and the octa-functionalized styrene silsesquioxane (OS-POSS) pushes the PS-*b*-P4VP block copolymer possessing to disorder morphology at higher OS-POSS content.[41] On the
85 contrary, the relative stronger hydrogen bonding in OP-POSS/PS-*b*-P4VP induce order–order transition from alternative lamellae to cylinder and finally to body-centered cubic sphere.[41]

As a result, we might expect strong hydrogen bonding interaction to enable relative higher loadings of nanoparticles
90 within the diblock copolymer segments. Based our knowledge, however, the hydrogen bonding strength influence on the self-assembly structures of diblock copolymers and nanoparticles have never been reported previously. In this study, we blended OP-POSS NPs with three well-established diblock copolymers—

Table 1: Molecular weights (M_n), compositions, and polydispersity indices (PDIs) of OP-POSS and the PS-*b*-P4VP, PS-*b*-P2VP, and PS-*b*-PMMA BCPs

BCP[a]	M_n (GPC)[b]	PS (wt%)[c]	PDI[b]	T_g (°C)[d]
PS$_{216}$-*b*-P4VP$_{257}$	49,450	48	1.12	106/152
PS$_{216}$-*b*-P2VP$_{268}$	49,950	42	1.03	108/108
PS$_{200}$-*b*-PMMA$_{252}$	55,300	40	1.06	110/135
OP-POSS	1978	-	1.00	18

[a] Numbers denote final compositions determined through gel permeation chromatography (GPC, calibrated against polystyrene linear standards) and integrated ^{1}H NMR spectra. [b] Measured using GPC. [c] Determined from ^{1}H NMR spectra. [d] Determined from DSC analyses.
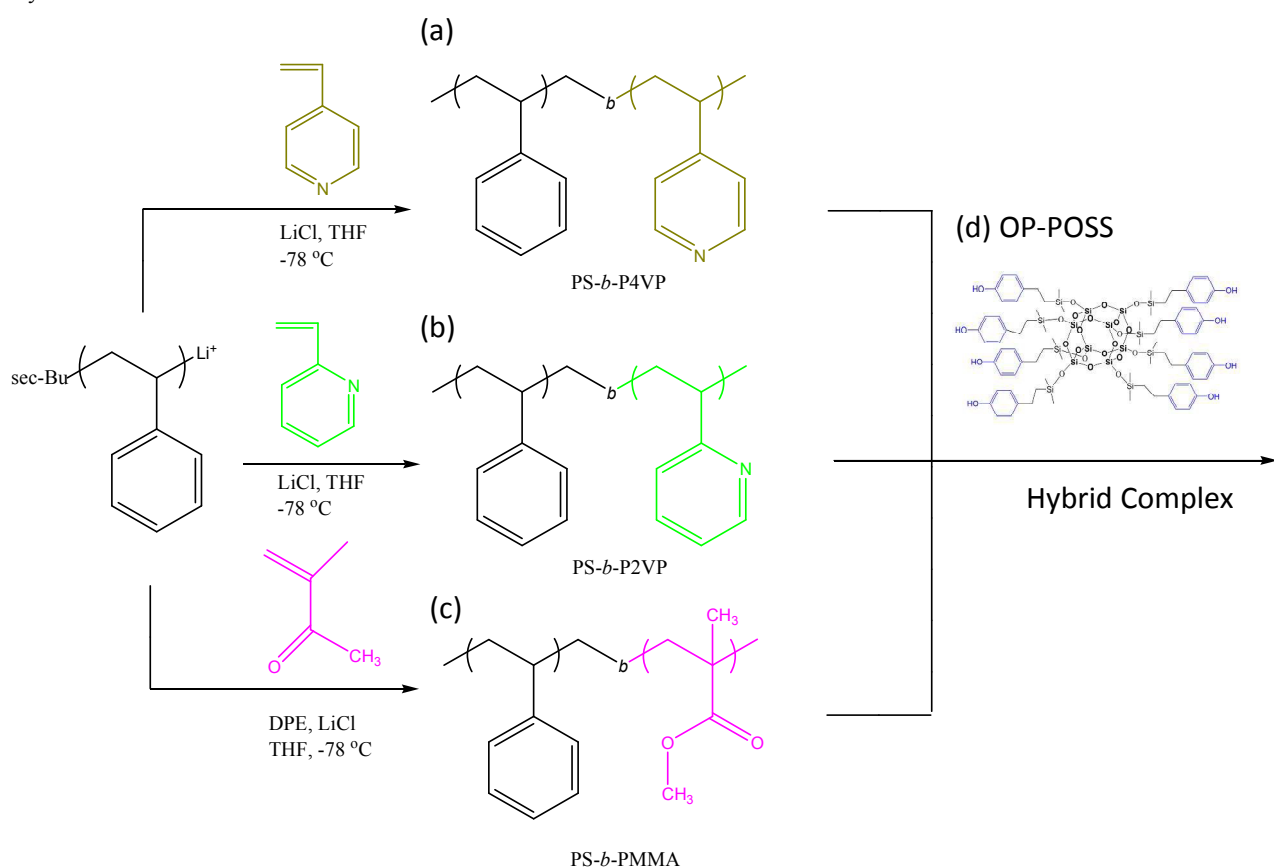
Scheme 1: The preparation of (a) PS-*b*-P4VP, (b) PS-*b*-P2VP, (c) PS-*b*-PMMA through anionic polymerization and the chemical structure of (d) OP-POSS

PS-*b*-PMMA, PS-*b*-P2VP, and PS-*b*-P4VP—formed through sequential anionic polymerization.[42] These three systems allowed us to make general predictions about how hydrogen bonding strength influences the structures of nanoparticles in block copolymers, with the goal of realizing multifunctional organic/inorganic hybrid materials. The inter-association equilibrium constants of P4VP/ poly(vinyl phenol) (PVPh) (K_A = 1200), P2VP/PVPh (K_A = 598), and PMMA/PVPh (K_A = 37.4), as well as the self-association equilibrium constant (K_B = 66.8) of PVPh were determined Based on the Painter–Coleman association model.[43–45] Therefore, the strengths of the hydrogen bonding interaction of P4VP, P2VP, and PMMA with OP-POSS follow the order P4VP/OP-POSS > P2VP/OP-POSS > PMMA/OP-POSS, with K_A/K_B > 1 for P4VP/OP-POSS and P2VP/OP-POSS and K_A/K_C < 1 for PMMA/OP-POSS.[42] In this present study, the miscibility behavior, intermolecular hydrogen

bonding interaction and self-assembly structures of these three hybrid complex system were investigated by using differential scanning calorimetry (DSC), Fourier transform infrared spectroscopy (FTIR), small-angle X-ray scattering (SAXS), and transmission electron microscopy (TEM) analyses.

Experimental Section
Materials
Styrene, 4-acetoxystyrene, 4-vinylpyridine, 2-vinypyridine, methyl methacrylate, and platinum(0)/1,3-divinyl-1,1,3,3-tetramethyldisiloxane complex solution [Pt(dvs)] were all obtained from Aldrich Chemical (USA). The diblock copolymers of PS$_{216}$-*b*-P4VP$_{257}$, PS$_{366}$-*b*-P2VP$_{220}$ and PS$_{200}$-*b*-PMMA$_{252}$ were all synthesized through sequential anionic polymerization as shown in Scheme 1.[42] OP-POSS (M_n = 1978 g/mol) was
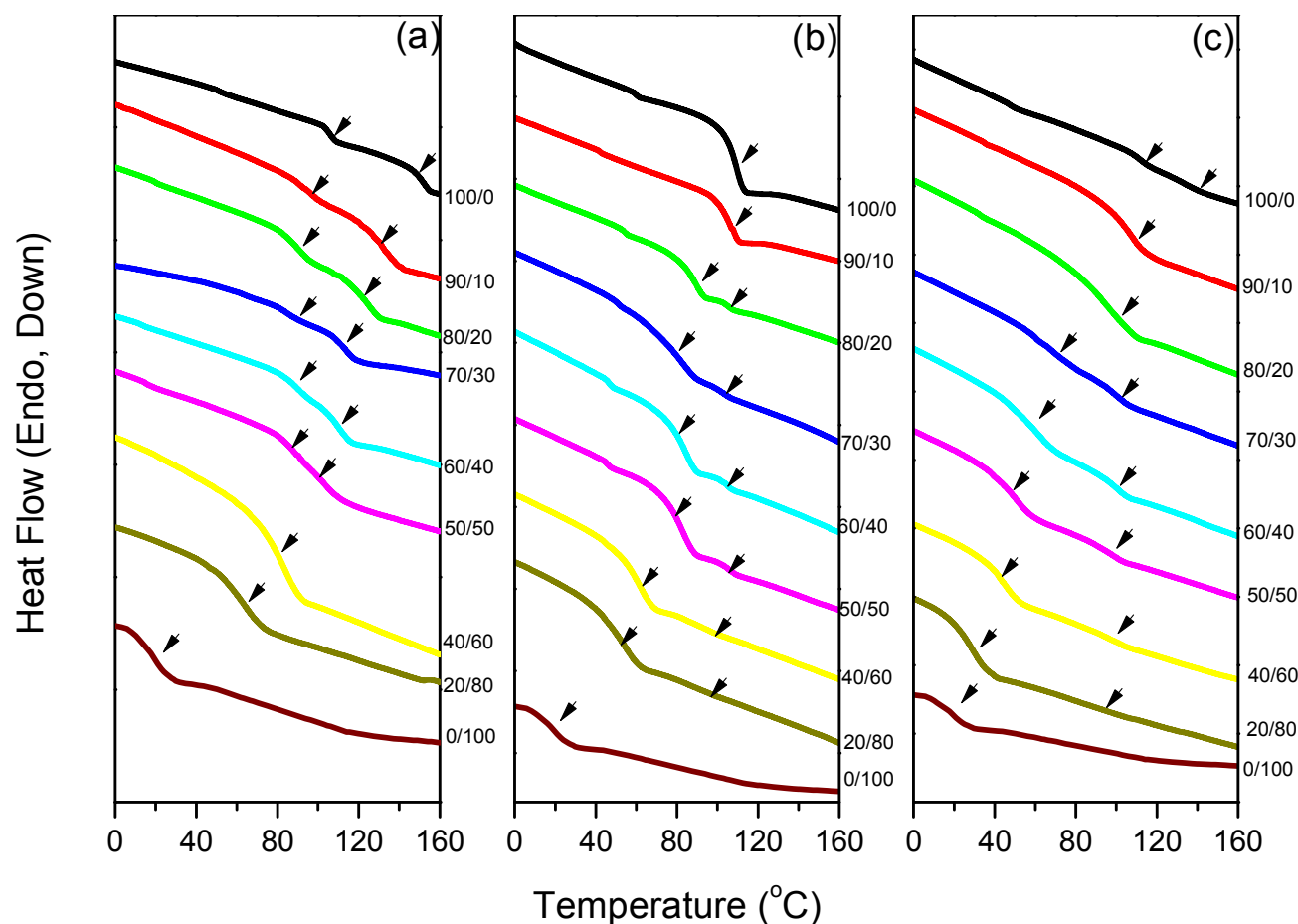
Figure 1: DSC analyses of (a) PS-*b*-P4VP/OP-POSS, (b) PS-*b*-P2VP/OP-POSS, and (c) PS-*b*-PMMA/OP-POSS complexes.
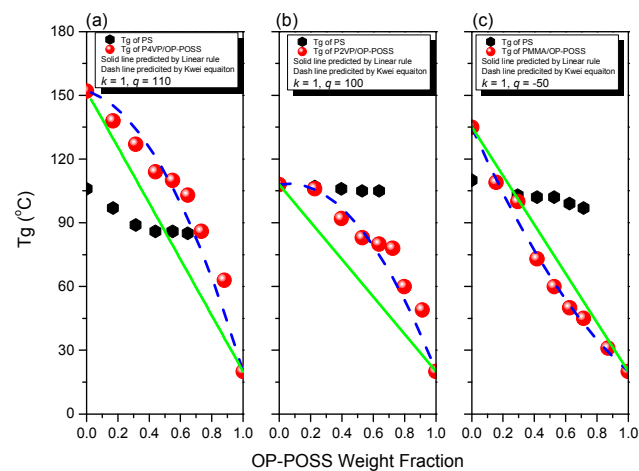
Figure 2: T_g behavior of (a) PS-*b*-P4VP/OP-POSS, (b) PS-*b*-P2VP/OP-POSS, and (c) PS-*b*-PMMA/OP-POSS complexes.

synthesized according to our previous studies.[46–49] Details of syntheses and characterizations of PS-*b*-P4VP, PS-*b*-P2VP, and PS-*b*-PMMA diblock copolymers are available elsewhere;[42–49] the characterization data for these materials are summarized in Table 1.

BCP/NP Blend

Blending OP-POSS NPs with various weight fractions of PS-*b*-

P4VP, PS-*b*-P2VP, and PS-*b*-PMMA block copolymers were prepared through solution blending. 5 wt% of the BCP/NPs blends in THF solution were stirred for 24 h and then cast on the Teflon pan. The THF solvent was slowly evaporated at room temperature for 2 day and then dried under the vacuum oven at 120 °C for 2 days.

Characterization

Thermal properties of the blend samples were determined by DSC analysis by using the TA Q-20 instrument; the instrument was operated at a 20 °C/min of heating rate from -90 °C to –200 °C under N_2; the weight of each blend samples was ca. 5~10 mg. FTIR spectra of blend samples were determined by using the conventional KBr disk method with the Bruker Tensor 27 FTIR spectrophotometer at room temperature. SAXS was performed using the NANOSTAR U small-angle X-ray scattering system (Bruker AXS, Karlsruhe, Germany) and Cu-Kα radiation (30 W, 50 kV, 600 mA). TEM observations were conducted by the JEOL 2100 microscope (Japan) operated at 200 kV. Ultrathin sample was prepared by using the Leica Ultracut S microtome equipped with the diamond knife. The BCP/NPs hybrid thin film without any staining was recorded for TEM images since the dark region was corresponding to POSS-rich domain due to the Si atom of POSS providing the relative higher mass contrast compared with the organic domains. The bright region is corresponding to the PS phase in the minor domain as would be expected.

Soft Matter
CREATED USING THE RSC ARTICLE TEMPLATE (VER. 3.0) - SEE WWW.RSC.ORG/ELECTRONICFILES FOR DETAILS
Page 4 of 13

ARTICLE TYPE   www.rsc.org/xxxxxx | XXXXXXXX
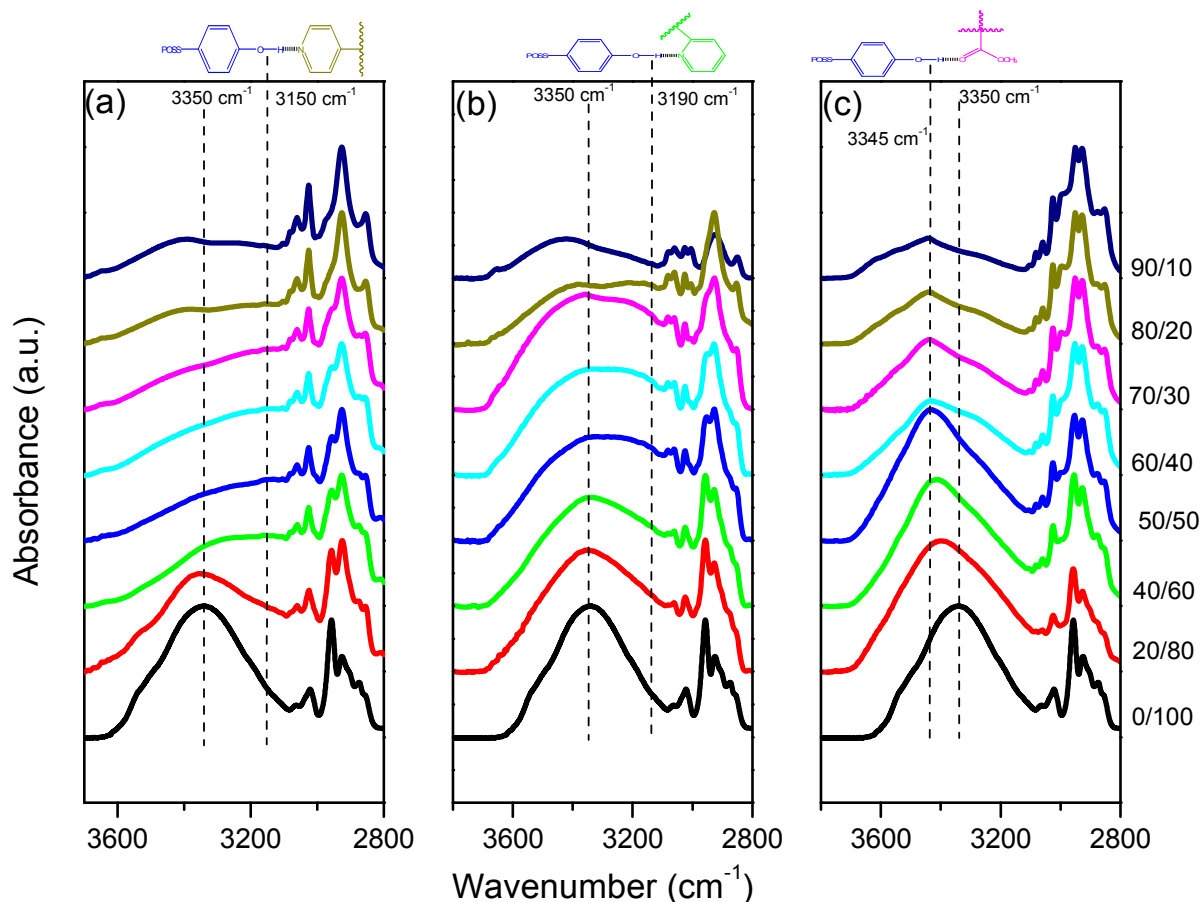
Figure 3: FTIR spectra of hydroxyl stretching region of (a) PS-*b*-P4VP/OP-POSS, (b) PS-*b*-P2VP/OP-POSS, and (c) PS-*b*-PMMA/OP-POSS complexes recorded at room temperature

Results and Discussion

Thermal Analyses

Figure 1 presents DSC analyses of PS-*b*-P4VP/OP-POSS, PS-*b*-P2VP/OP-POSS, and PS-*b*-PMMA/OP-POSS blends with various compositions. Clearly, the glass transition temperature of the pure OP-POSS NP is ca. 18 °C[46] and the pure PS-*b*-P4VP block copolymer displayed two glass transition temperatures at 106 °C and 152 °C, corresponding to PS and P4VP block segment, respectively.[41] The pure PS-*b*-P2VP diblock copolymer displayed only one single glass transition temperature of approximately 108 °C, as might be expected because pure PS and pure P2VP both display similar glass transition temperatures near this value.[50] In contrast, the pure PS-*b*-PMMA diblock copolymer also experienced two glass transition temperatures: a lower value of T_g near 116 °C (resulting from the PS segments) and a higher value near 135 °C (resulting from the PMMA segments), which is higher than pure PMMA homopolymer (ca. 100 °C), as has also been discussed in a previous study.[51] Notably, the T_g value of PS blocks (106–116 °C) in these three BCPs are higher than PS homopolymer (~100 °C) of similar molecular weight since the nano-confinement effect.

In Figure 1(a), we also observe two values of T_g at relatively lower OP-POSS contents (< 50 wt%). Here, the lower value (85–106 °C) was assigned corresponding to the PS domain and the higher value (103–152 °C) from the hydrogen-bonded P4VP/OP-POSS complex domain. The single but broad T_g

observed at ca. 86 °C was due to the T_g behavior of PS domain and P4VP/OP-POSS complex domain by coincidence decreased to the similar temperature range. Two Tg behaviors reappear at 80 wt% OP-POSS NPs was from P4VP/OP-POSS complex domain (63 °C) and the higher one (90 °C) was corresponding to PS domain.[41] In Figure 1(b), although the pure PS-*b*-P2VP diblock copolymer and PS-*b*-P2VP/OP-POSS = 90/10 both displayed only the single glass transition temperature near 108 °C. Increasing to 20 wt% or more OP-POSS contents show two glass transition temperatures; the lower one (50–90 °C) was from the hydrogen-bonded P2VP/OP-POSS domain and the higher one (100–108 °C) was corresponding to PS block segment. In Figure 1(c), the pure PS-*b*-PMMA diblock copolymer also experienced two glass transition temperatures, but at 10 and 20 wt% of OP-POSS, we observed only a single glass transition temperature in each case, near 109 and 103 °C, respectively. The reason for this behavior is similar to PS-*b*-P4VP/OP-POSS complexes: the T_g of PMMA/OP-POSS complex domain dropped to the similar glass transition temperature range of PS domain. As a result, further increase OP-POSS contents higher than 30 wt% also observe two T_g values to reappear again: the lower one (31–73 °C) was corresponding to the PMMA/OP-POSS complex domain through hydrogen bonding and the higher one (95-102 °C) was corresponding to the PS domain. In these three hybrid systems, we did not observe the single T_g for pure OP-POSS at 18 °C, indicating that no macrophase aggregation of OP-POSS NPs due
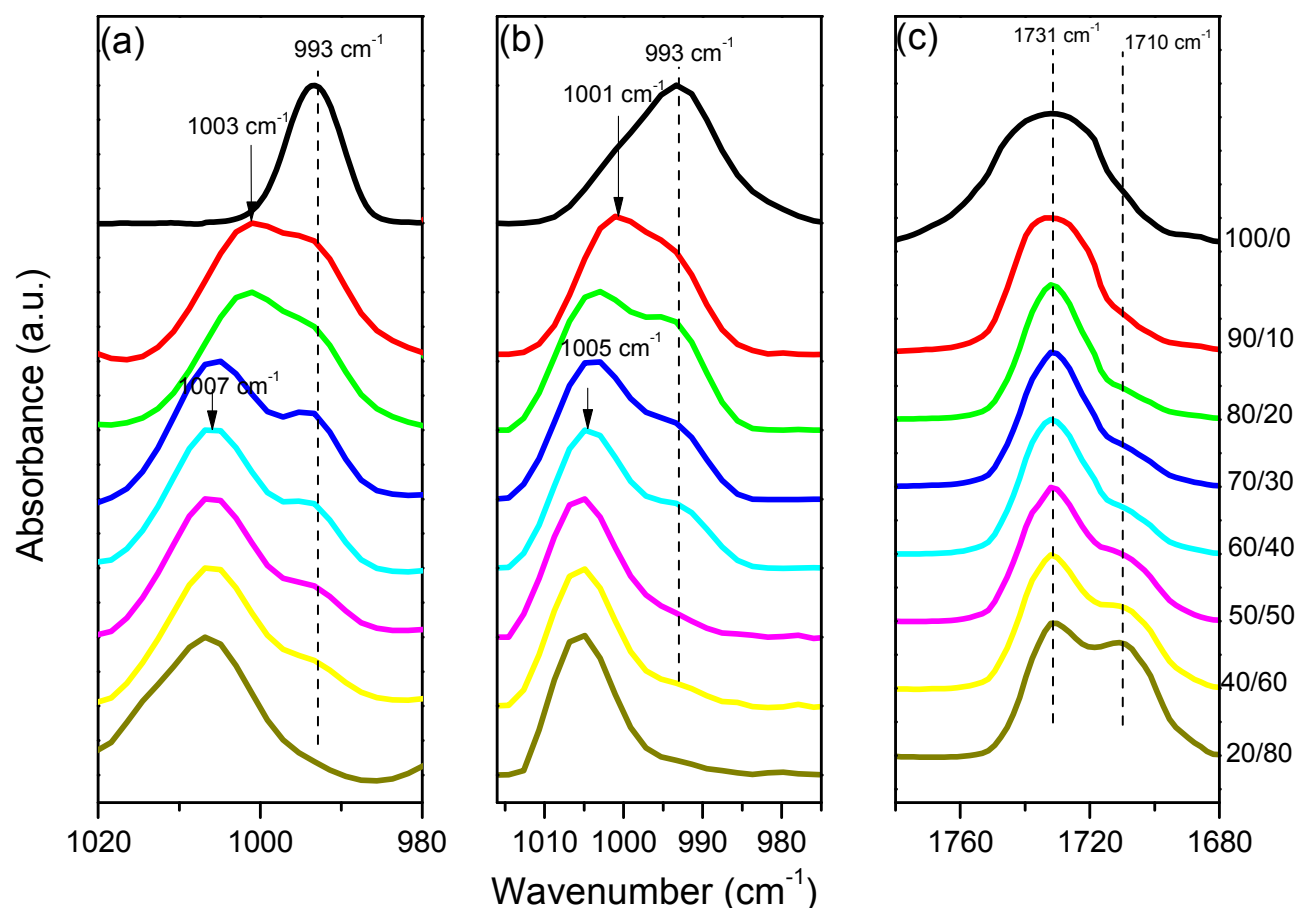
Figure 4: FTIR spectra of (a) PS-*b*-P4VP/OP-POSS (pyridine region), (b) PS-*b*-P2VP/OP-POSS (pyridine region), and (c) PS-*b*-PMMA/OP-POSS (C=O region) hybrid complexes at room temperature
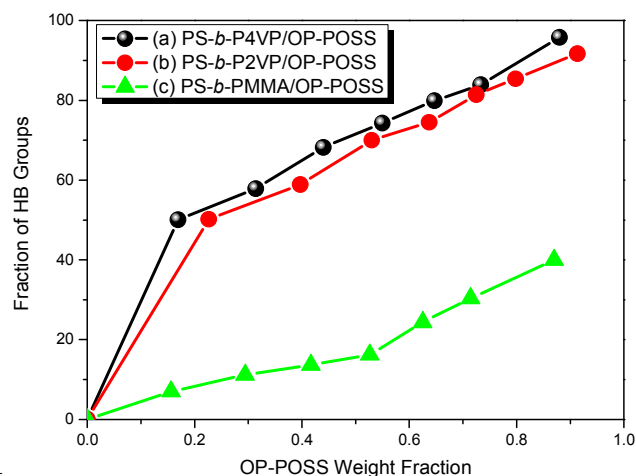
Figure 5: Fractions of hydrogen-bonded functional groups of (a) PS-*b*-P4VP/OP-POSS (pyridine region), (b) PS-*b*-P2VP/OP-POSS (pyridine region), and (c) PS-*b*-PMMA/OP-POSS (C=O region) hybrid complexes.

to the existing intermolecular hydrogen bonding between the phenolic hydroxyl (OH) groups of OP-POSS with the pyridine groups of P4VP/P2VP and with the carbonyl (C=O) groups of PMMA.

Figure 2 summarizes the T_g behavior of P4VP/OP-POSS, P2VP/OP-POSS, and PMMA/OP-POSS complex systems. Interestingly, the T_g behavior of the P4VP/OP-POSS and

P2VP/OP-POSS complex domains exhibit the positive deviation compared with the linear rule, whereas the OP-POSS/PMMA complex domain exhibit the negative deviation. We employed the Kwei equation[52] to characterize specific interaction blending systems:

$$T_g = \frac{W_1 T_{g1} + k W_2 T_{g2}}{W_1 + k W_2} + q W_1 W_2 \qquad (1)$$

Where W_i and T_{gi} are the weight fractions and glass transition temperatures of each components, k and q are the fitting constants. The values of ($k =1$, $q = 110$) for P4VP/OP-POSS complex [Figure 2(a)], ($k =1$, $q = 100$) for P2VP/OP-POSS complex [Figure 2(b)], and ($k =1$, $q = -50$) for the PMMA/OP-POSS complex [Figure 2(c)] are obtained based on the non-linear leas-squares best fitting. The positive q values suggest that P4VP/OP-POSS and P2VP/OP-POSS complex possessing with stronger inter-association hydrogen bonding than the self-association hydrogen bonding of OP-POSS. On the contrary, the inter-association hydrogen bonding of PMMA/OP-POSS complex is weaker than the self-association hydrogen bonding of OP-POSS and then results in the negative q value. In addition, the q value of P4VP/OP-POSS complex is larger than P2VP/OP-POSS hybrid complex, due to steric hindrance affecting the hydrogen bonding interaction strength.[50,53] Therefore, the hydrogen bonding interactions strengths in these systems follow the order of P4VP/OP-POSS > P2VP/OP-POSS > PMMA/OP-POSS, consistent with the values of K_A based on the Painter–Coleman association model: 1200 for P4VP/PVPh, 598 for P2VP/PVPh, and 37.4 for PMMA/PVPh.[46]
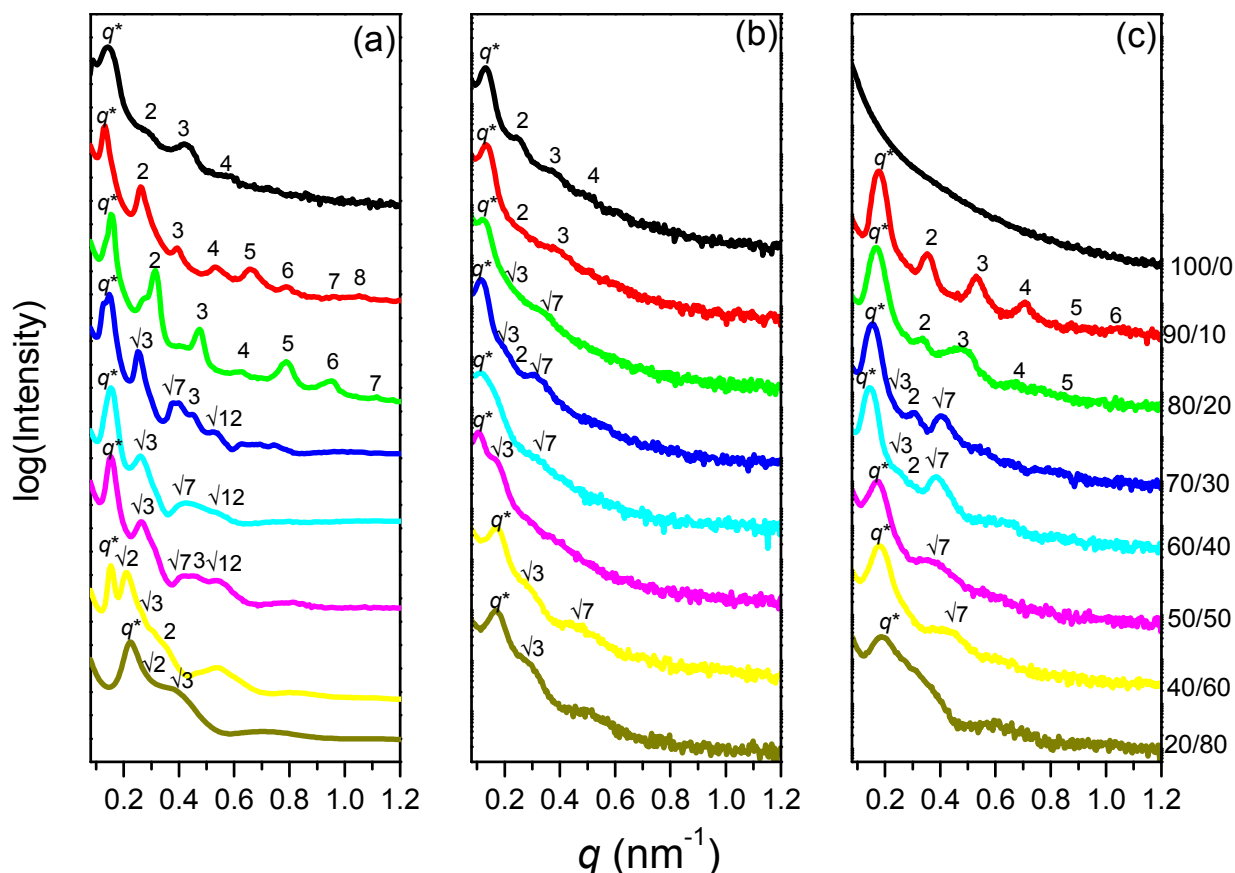
Figure 6: SAXS patterns of (a) PS-*b*-P4VP/OP-POSS, (b) PS-*b*-P2VP/OP-POSS, and (c) PS-*b*-PMMA/OP-POSS hybrids at room temperature

In addition, the T_g value of PS block segment was decreased with the increase of OP-POSS NPs contents due to the lower Tg value of OP-POSS NPs.

Infrared Spectroscopic Analyses

Figure 3 shows the infrared spectra of PS-*b*-P4VP/OP-POSS, PS-*b*-P2VP/OP-POSS, and PS-*b*-PMMA/OP-POSS complexes at room temperature. The OP-POSS possessing two major absorption peaks in the hydroxyl (OH) stretching region: one is corresponding to the free hydroxyl group at 3525 cm^{-1} and the other broader band is centered at ca. 3350 cm^{-1} due the self-association hydrogen-bonded hydroxyl-hydroxyl (OH-OH) groups. Clearly, the intensity of free hydroxyl group of OP-POSS was decreased with the increase of PS-*b*-P4VP, PS-*b*-P2VP, and PS-*b*-PMMA contents. Meanwhile, the broad band peak was shifted to the relative lower wavenumber with the increase of PS-*b*-P4VP and PS-*b*-P2VP contents, reflecting a redistribution of hydrogen bonds from self-association hydroxyl-hydroxyl interaction to inter-association hydroxyl-pyridine interaction and thus we can assign the peak at 3150 cm^{-1} in Figure 3(a) corresponding to the hydrogen bonding between phenolic OH group of OP-POSS and the pyridine group of P4VP block, and the band at 3190 cm^{-1} in Figure 3(b) corresponding to OH-pyridine between OP-POSS and P2VP block. In contrast, the broad signal for the hydrogen-bonded hydroxyl groups of OP-POSS was shifted to higher wavenumber (3430 cm^{-1}) at the highest PS-*b*-PMMA content (80 wt%) [Figure 3(c)]. This phenomenon also suggests the new distribution of hydrogen bonds from competition between OH-OH of OP-POSS and OH-O=C of OP-POSS/PMMA complex. We used the frequency difference ($\Delta\nu$) between the free hydroxyl and intermolecular hydrogen bonded hydroxyl group signals to determine the average hydrogen bonding interaction strength.[54] We found the P4VP/OP-POSS ($\Delta\nu = 375$ cm^{-1}), P2VP/OP-POSS ($\Delta\nu = 335$ cm^{-1}) were both stronger than that of self-association of OH-OH for OP-POSS ($\Delta\nu = 185$ cm^{-1}). As a result, the values of q are positive, based on the Kwei equation (Figure 2). In contrast, the PMMA/OP-POSS ($\Delta\nu = 95$ cm^{-1}) is weaker than self-association of OH-OH for OP-POSS and thus, the q value is negative, based on the Kwei equation (Figure 2).

In addition to hydroxyl stretching, the pyridine groups of P4VP and P2VP and the carbonyl group of PMMA are also sensitive to the hydrogen bonding interaction. In general, the band at 993 cm^{-1} is able to characterize the intermolecular hydrogen bonding of pyridine groups of P4VP and P2VP block segment. Figures 4(a) and 4(b) present infrared spectra at the range of 980–1020 cm^{-1} for PS-*b*-P4VP/OP-POSS and PS-*b*-P2VP/OP-POSS, respectively. Clearly, pure P4VP and P2VP blocks show the characteristic band at 993 cm^{-1}, due to the free pyridine group. A new band was found at 1007 and 1005 cm^{-1} due the hydrogen-bonded pyridine groups for the P4VP and P2VP block segments, respectively, when blending with OP-POSS NPs. We also found that the intermolecular hydrogen bonding strength in the P4VP/OP-POSS complex is stronger than in the P2VP/OP-POSS complex, due to steric hindrance affecting the specific interactions between these two polymers, as evidenced through different shifts in these wavenumbers (for P4VP, 14 cm^{-1}; for P2VP, 12 cm^{-1}).[50] In addition, the carbonyl group of PMMA block segment was split into two bands in Figure 4(c): one at 1731 cm^{-1} due the free carbonyl groups in PS-

ARTICLE TYPE
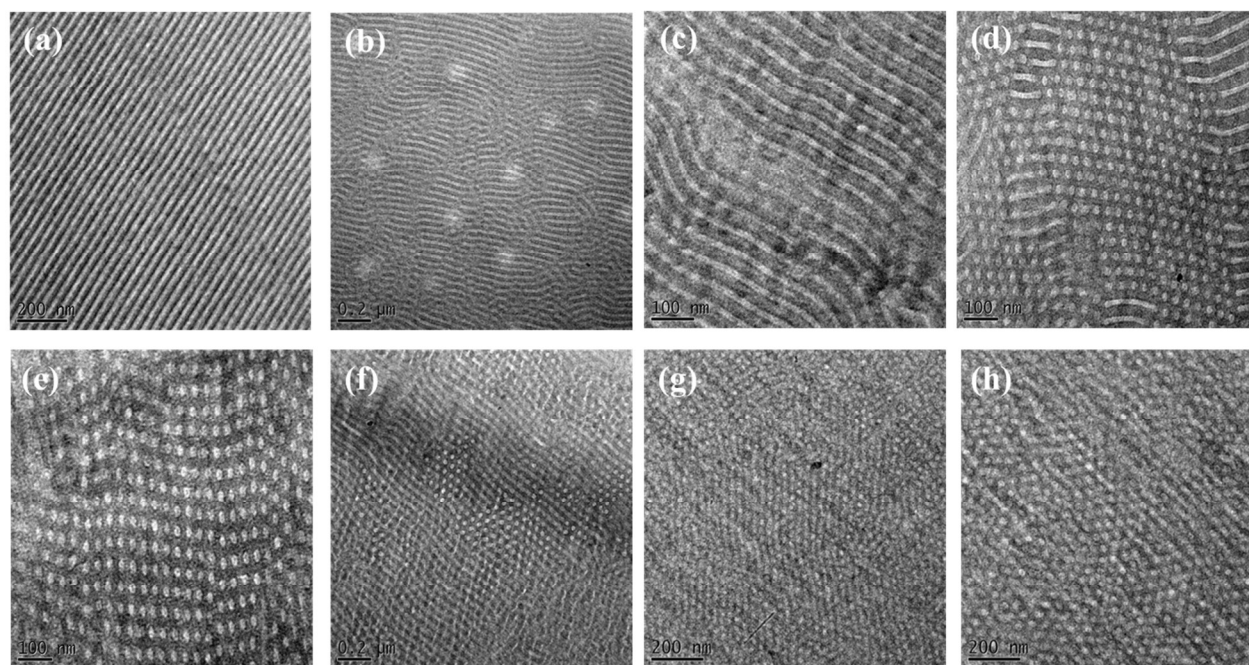
Figure 7: TEM images of PS-*b*-P4VP/OP-POSS complex of (a) pure PS-*b*-P4VP, (b) 10, (c) 20, (d) 30, (e) 40, (f) 50, (g) 60, and (h) 80 wt% OP-POSS contents

b-PMMA and the other at 1710 cm^{-1} due to the hydrogen-bonded ones. All pyridine and carbonyl group signals are able to split into two Gaussian bands that could be fitted well. Figure 5 summarizes the curve fitting results and we observed the fraction of hydrogen-bonded pyridine groups of P4VP and P2VP and carbonyl groups of PMMA was increased up increasing OP-POSS content in these three hybrid complexes, which is similar with P4VP, P2VP, and PMA blending with phenolic resins.[50,55,56] In addition, Figure 5 also shows that the fraction of hydrogen-bonded functional units also followed the order of P4VP/OP-POSS > P2VP/OP-POSS > PMMA/OP-POSS, consistent with the DSC analyses. The hydrogen-bonded fraction in P4VP/OP-POSS was slightly higher than that in P2VP/OP-POSS, due to the effect of steric hindrance in these two hybrid systems.

SAXS and TEM Analyses

Figure 6 shows SAXS profiles of PS-*b*-P4VP/OP-POSS, PS-*b*-P2VP/OP-POSS, and PS-*b*-PMMA/OP-POSS blends with various compositions at room-temperature. The long-range order of alternative lamellar structure was found for pure PS-*b*-P4VP [Figure 6(a)] based on the scattering ratios with1:2:3:4. The long period of this lamellar phase was ca. 45.1 nm based on the first SAXS at a position of $q = 0.139$ nm^{-1}, extracted from $2\pi/q$ equation. The TEM image in Figure 7(a) also shows the long-range order of alternating lamellar morphology for the pure PS-*b*-P4VP block possessing the alternative lamellar period ca. 40 nm, similar with SAXS analysis as shown in Figure 6(a). Adding 10 or 20 wt% OP-POSS contents, more long ranger order of scattering peaks was observed compared with pure PS-*b*-P4VP, with peak ratios of 1:2:3:4:5:6:7:8, corresponding to the lamellar structures, as confirmed by TEM images in Figures 7(b) and 7(c). Furthermore, the first scattering peak was shifted to the lower-*q* value slightly at 10 wt% OP-POSS content ($q_{max} = 0.127$ nm^{-1}; $d = 49.4$ nm), indicating the increase of the inter-lamellar spacing *D*. This peak shift to higher *q* value at 20 wt% OP-POSS content ($q_{max} = 0.151$ nm^{-1}; $d = 41.5$) was observed. At 20 wt% composition, it will transfer to hexagonal packed cylindrical

structure and further increasing to 30 wt% OP-POSS content, the morphology change from alternative lamellar to hexagonal packed cylindrical structures was occurred with $d = 41.5$ nm. This order–order transition was due to the overall volume fraction change between these two diblock copolymer segments. The peak ratios did not change with the 1:√3:√4:√7:√9:√12 ratio corresponding to long range order of hexagonal packed cylinder structures at 30, 40, and 50 wt% OP-POSS contents, this behavior was confirmed by TEM images as shown in Figures 7(d)–(f). The BCC symmetry spherical structure was observed as the OP-POSS content was at 60 and 80 wt% based on SAXS peaks with ratio of 1:√2:√3:√4, consistent with the TEM image as shown in Figures 7(g)-(h). The order-order transition from alternative lamellae to hexagonally packed cylinder and finally to BCC sphere upon increasing OP-POSS contents was observed based on SAXS and TEM analyses in PS-*b*-P4VP/OP-POSS complex.

Similarly, SAXS analysis also shows the lamellar structure for pure diblock copolymer of PS-*b*-P2VP [Figure 6(b)], also judging from the scattering peak ratio of 1:2:3:4. The SAXS peak located at first *q* value of 0.131 nm^{-1} with $d = 47.9$ nm for lamellae structure. The PS volume fraction is 42 % for this PS-*b*-P2VP diblock copolymer with the lamellar structure. TEM image in Figure 8(a) shows pure PS-*b*-P2VP diblock copolymer indeed exhibiting the short-range-ordered lamellar morphology. At 10 wt% OP-POSS content, SAXS pattern retained this lamellar structure with a relative peak ratio of 1:2:3, as confirmed by TEM image as shown in Figure 8(b). The first scattering peak was shifted to the lower-*q* region slightly at 10 wt% OP-POSS ($q_{max} = 0.129$ nm^{-1}; $d = 48.6$ nm), also implying the increase *d*-spacing of inter-lamellae. Further increasing to 20–50 wt% OP-POSS contents, the lamellar was transformed into cylinder structures with *d*-spacings of 49.4, 53.2, 55.1, and 59.2 nm, respectively, which showed the 1:√3:√4:√7 ratio for cylinder structures; as confirmed by TEM images in Figures 8(c)–(f). Further increasing to 60 and 80 wt% OP-POSS contents, the SAXS patterns showed a ratio of 1:√3:√7 and the *d*-spacings decreased to 37.4 nm (60 wt%) and 35.7 nm (80 wt%), implying the short-range-ordered
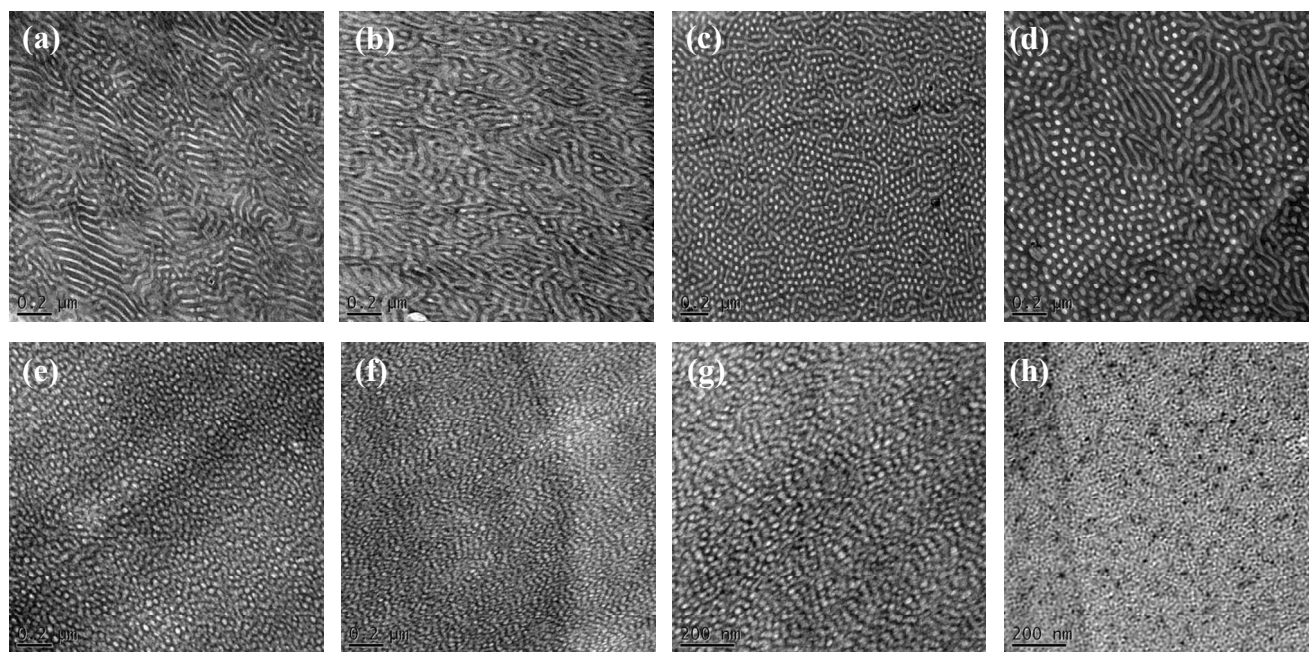
Figure 8: TEM images of PS-*b*-P2VP/OP-POSS complex of (a) pure PS-*b*-P2VP, (b) 10, (c) 20, (d) 30, (e) 40, (f) 50, (g) 60, and (h) 80 wt% OP-POSS contents

spherical micelle structure, as confirmed by TEM images in Figures 8(g) and 8(h), respectively. Similarly, the morphological transition also occurred with the increase of OP-POSS contents in PS-*b*-P2VP diblock copolymer. In contrast, because the hydrogen bonding in the P2VP/OP-POSS complexes was weak relative to the P4VP/OP-POSS complexes, the former system formed disordered structures at relatively higher OP-POSS contents (>60 wt%).

SAXS analysis showed a disordered and phase-mixed structure for pure PS-*b*-PMMA in Figure 6(c); TEM imaging supported the presence of a phase-mixed structure [Figure 9(a)]. It is well established that PS-*b*-PMMA diblock copolymers show an upper disorder–order transition (UDOT) and that the the interaction parameter (χ) is quite weak.[57-58] In addition, the degree of polymerization ($N = 452$) of the PS-*b*-PMMA dblock copolymer used in this study was not particularly high; thus, at low values of χN, the PS-*b*-PMMA was phase-mixed.[57,58] Nevertheless, after adding 10 wt% OP-POSS content into the PS-*b*-PMMA (7% of C=O groups interacted with OP-POSS), sharp scattering patterns appeared with relative peak ratio of 1:2:3:4:5:6, having the long period of lamellar structure of 35.2 nm; the TEM image in Figure 9(b) confirmed the such structure. Further increasing to 20 wt% OP-POSS content (11.2% of C=O groups interacted with OP-POSS), the scattering pattern remained sharp with relative peak ratio of 1:2:3:4:5, also suggesting the long-range-ordered lamellar structures, as confirmed by the TEM image in Figure 9(c). The first scattering peak was also shifted to the lower-*q* region slightly ($q_{max} = 0.165$ nm^{-1}; $d = 38.0$ nm), again implying the increase *d*-spacing of inter-lamellae. Russell et al. have reported that the increase of segmental interaction parameter (χ) between PS and PMMA by the formation of PMMA-lithium ionic complexes; they also found that the PS-*b*-PMMA diblock copolymer shows the morphology from the phase-mixed to the microphase-separation structure after the formation of PMMA-lithium ionic complexes.[59,60]

In this study, intermolecular hydrogen bonding existed between the phenolic hydroxyl groups of OP-POSS and the carbonyl groups of PMMA, also increasing the segmental interaction parameter between PS and PMMA and by an effective increase in molecular weight by physical cross-linking through hydrogen bonding and, therefore, increasing the value of χN. As a result, we found that the change in morphology from a phase-mixed to a long-range-ordered lamellar structure occurred when adding only 10 or 20 wt% OP-POSS. Further increasing to 30 and 40 wt% OP-POSS contents, the transition occurred from the alternative lamellar to the cylinder structure with the *d*-spacing of 39.0 and 43.3 nm, respectively, as revealed from the 1:$\sqrt{3}$:$\sqrt{4}$:$\sqrt{7}$ ratio expected for cylindrical structures; the TEM images in Figures 9(d)–(e) confirmed this behavior. Further increase the OP-POSS NP content at 50 and 60 wt%, the SAXS patterns showed a ratio of 1:$\sqrt{7}$ and the *d*-spacings decreased to 36.3 nm (50 wt%) and 34.5 nm (60 wt%), respectively, indicating that the morphologies of these samples featured short-range-ordered wormlike structure, as confirmed by the TEM images in Figures 9(f) and 9(g), respectively. When the OP-POSS content at 80 wt%, it resulted in the broad peak, with the *d*-spacing decreasing further to 31.5 nm, corresponding to a disordered micelle or macrophase-separated structure, as confirmed by the TEM image as shown in Figure 9(h).

The distributions of OP-POSS NPs in these three complexes were investigated in this study. The average distance of a_J for the chemical junction of the block copolymer interface and the relative changes of a_J/a_{J0} are able to derive for the complexes where a_{J0} is corresponding to the pure diblock copolymer. The values of D/D_0 of $(\rho_J/\rho_{J0})\Phi_{block}{}^{-1}$ are simple volumetric conversion for the lamellar strucutre, $(\rho_J/\rho_{J0})[(2/3^{1/2})\pi(1-f)\Phi_{block}{}^{-1}]^{1/2}$ for the cylindrical structure, and $(\rho_J/\rho_{J0})[(27\sqrt{3}/8)\pi(1-f)^2\Phi_{block}^{-1}]^{1/2}$ for body center cubic spherical structure. D_0 is the inter-distance of pure diblock copolymer, f is the PS block volume fraction, and ρ_J is corresponding to block chain number per unit interfacial area
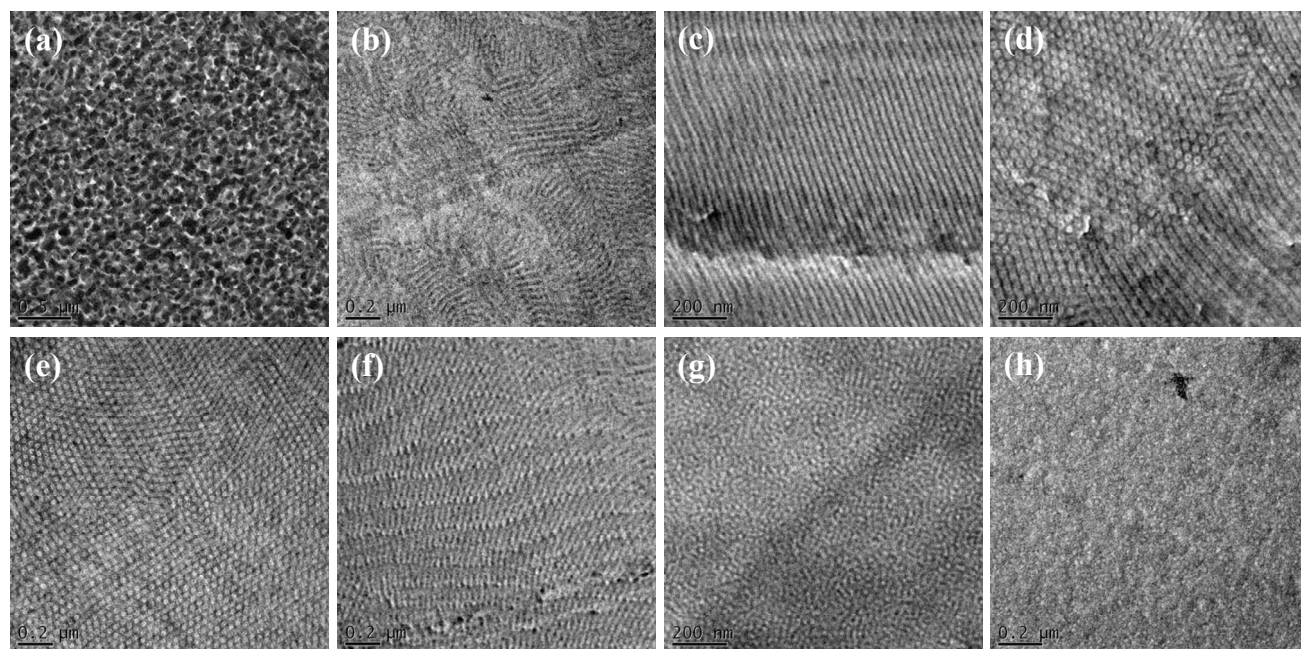
Figure 9: TEM images of PS-*b*-PMMA/OP-POSS complex of (a) pure PS-*b*-PMMA, (b) 10, (c) 20, (d) 30, (e) 40, (f) 50, (g) 60, and (h) 80 wt% OP-POSS contents
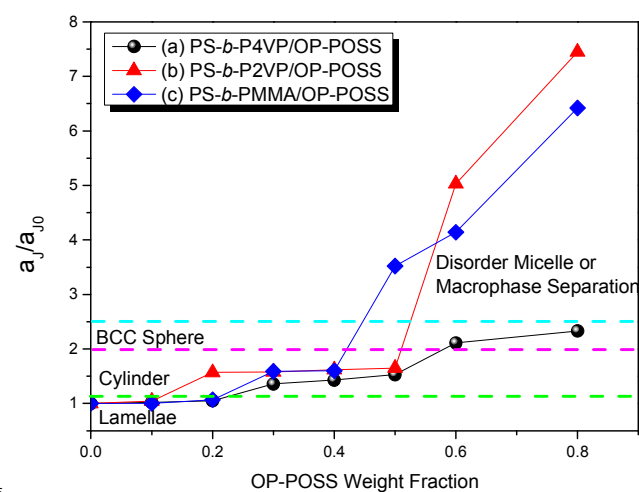
Figure 10: Average distances of the chemical junctions along the interface, a_J/a_{J0}, for (a) PS-*b*-P4VP/OP-POSS, (b) PS-*b*-P2VP/OP-POSS, and (c) PS-*b*-PMMA/OP-POSS complexes

(a_J^2); thus, a_J/a_{J0} is equal to $(\rho_J/\rho_{J0})^{-1/2}$ and Φ is the volume fraction of BCPs in complexes.[31,32] Figure 10 summarizes the a_J/a_{J0} values in these three hybrid system with various OP-POSS contents based on above three relations. We observed the expansion in the a_J values of $(a_J/a_{J0} >1)$ for all three hybrid systems—presumably the result of the additive OP-POSS intervening and wetting the P4VP, P2VP, and PMMA chains of the BCPs at the interfaces through hydrogen bonding. We consider no change in BCP/NPs density since the PS block covalently linked to the hydrogen bonded acceptor blocks of P4VP, P2VP, and PMMA segment, which have to contract to accommodate in the expanded interfacial zone.

The values of a_J/a_{J0} for the P4VP/P4VP complexes increased from 1.02 (at 10 wt% OP-POSS) to 2.35 (at 80 wt% OP-POSS). Scheme 2(a) summarizes the morphological transformation of

PS-*b*-P4VP that occurred upon increasing the OP-POSS contents. Pure PS-*b*-P4VP shows the long-range order of alternative lamellar structure by increasing the OP-POSS contents to 10 and 20 wt% remains the lamellar structure. Further increasing to 30–50 wt% OP-POSS contents changed to cylindrical structures and corresponding the *d*-spacing increase, with values of a_J/a_{J0} of 1.35, 1.42, and 1.52 for the blends having OP-POSS contents of 30, 40, and 50 wt%, respectively. At 60 wt% and 80 wt% OP-POSS content, BCC spheres formed and the *d*-spacing decreased significantly, providing a value of a_J/a_{J0} is 2.06 and 2.35, respectively. This order–order transition from lamellae to cylinder and finally to BCC sphere was come from the relative stronger hydrogen bonding interaction between the phenolic hydroxyl groups of OP-POSS and pyridine groups of P4VP and then changed the overall volume fractions of block copolymer segments.

Scheme 2(b) summarizes the morphological transformation of PS-*b*-P2VP diblock copolymer upon increasing the OP-POSS contents. Pure PS-*b*-P2VP shows a lamellar structure; at 10 wt% OP-POSS NP content, the lamellar structure was maintained, with a value of a_J/a_{J0} of 1.04. When the OP-POSS contents at 20-50 wt%, these composition changed to cylindrical structures and corresponding increases in the *d*-spacing, with values of a_J/a_{J0} of 1.57, 1.58, 1.62, and 1.65 at OP-POSS contents of 20, 30, 40, and 50 wt%, respectively. Further increasing OP-POSS NP contents to 60 and 80 wt%, the *d*-spacings decreased, with the values of a_J/a_{J0} increasing significantly to 5.03 and 7.45, respectively, when using the sphere model. This phenomenon could be explained as the result of a short-range-ordered spherical micelle structure forming at these compositions; the curvature changed significantly and then increased the value of a_J/a_{J0}. Because the hydrogen bonding in PS-*b*-P2VP/OP-POSS complexes was weaker than that of P4VP/OP-POSS complexes, because of steric hindrance effect, the former system formed close-to-disordered structures at relative higher OP-POSS contents (> 60 wt%).

Scheme 2(c) also summarizes the morphological transformation of PS-*b*-PMMA upon increasing the OP-POSS
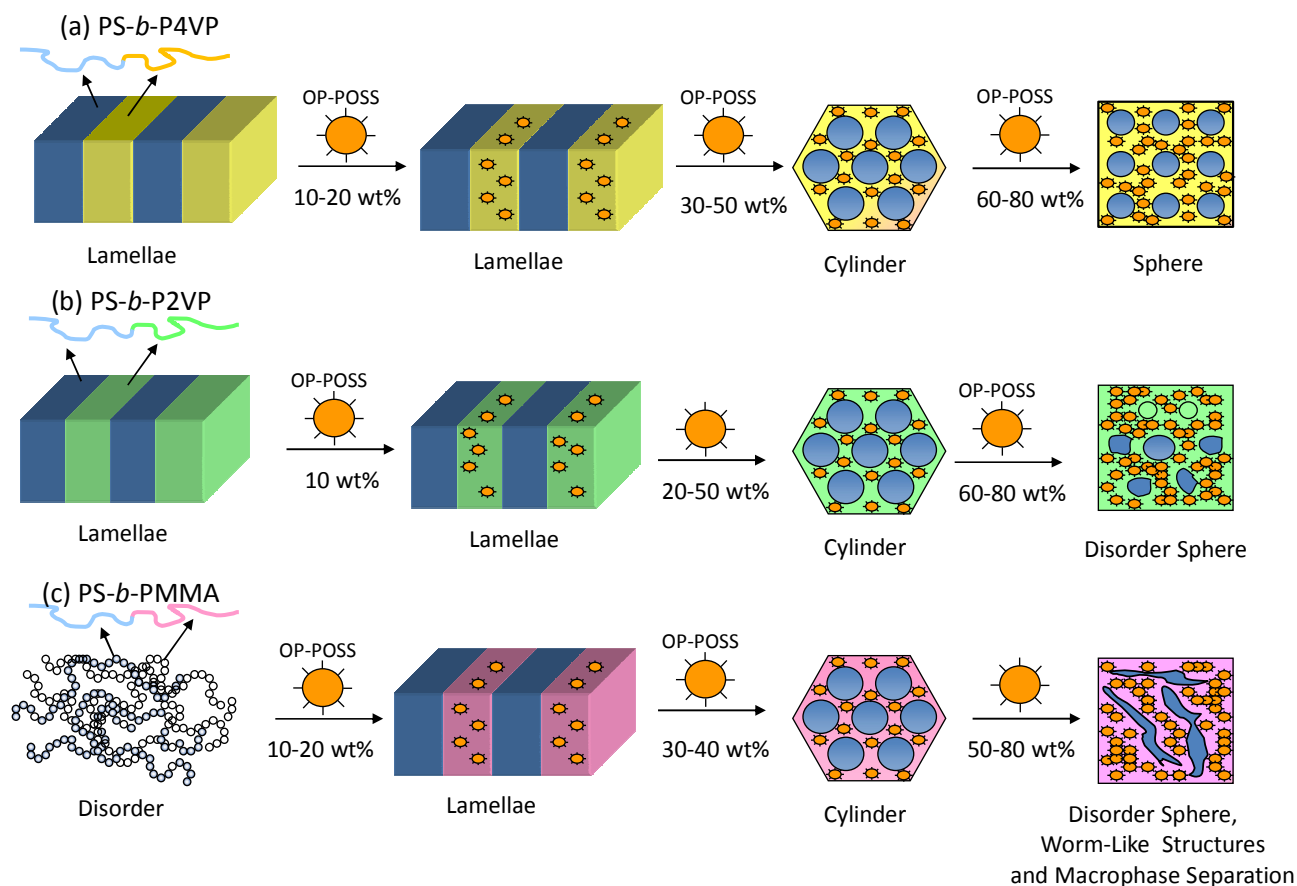
Scheme 2: Morphological transition of (a) PS-*b*-P4VP/OP-POSS, (b) PS-*b*-P2VP/OP-POSS, and (c) PS-*b*-PMMA/OP-POSS complexes with the increase of OP-POSS contents

5 contents. Pure PS-*b*-PMMA shows a phase-mixed structure because of the lower value of χN. When the OP-POSS NP contents were at 10 and 20 wt%, the phase-mixed structure was changed to long-range order of alternative lamellar structures because of hydrogen bonding interaction between the phenolic 10 hydroxyl groups of OP-POSS and the carbonyl groups of PMMA and thus increased the interaction parameter between PS and PMMA block segment and then increased the value of χN. Because the pure PS-*b*-PMMA diblock copolymer possessed a phase-mixed structure, we could not determine a value of D_0. For 15 comparison, we chose a value of D_0 of 35.2 nm for the system of 10 wt% OP-POSS content in PS-*b*-PMMA; thus, the value of a_J/a_{J0} was 1.07 for the system containing 20 wt% OP-POSS. Further increasing to 30-40 wt% OP-POSS contents were changed to cylindrical structures and corresponding increases in 20 *d*-spacings, with values of a_J/a_{J0} of 1.59 and 1.60 at OP-POSS contents of 30 and 40 wt%, respectively. When the OP-POSS NP contents were 50, 60, and 80 wt%, the *d*-spacings decreased and the values of a_J/a_{J0} increased significantly to 3.52, 4.14, and 6.42, respectively, when using the sphere model. This phenomenon can 25 be explained as arising from short-range-ordered spherical micelles or macrophase-separated structures at these compositions. Because the PS-*b*-PMMA/OP-POSS complexes experienced the weakest hydrogen bonding among these three systems, they formed close-to-disordered structures at only 50 30 wt% OP-POSS content.

In summary, at relatively low OP-POSS contents (ca. 10–20 wt%), these hybrid systems almost all formed lamellae structures with lower values of a_J/a_{J0} (<1.07), with the OP-POSS NPs

displaying wet-brush behavior for each of these three diblock 35 copolymers. When the OP-POSS contents were approximately 30–40 wt%, order-order transition behavior occurred, from lamellae to hexagonally packed cylinder structures, with values of a_J/a_{J0} between 1.35 and 1.65, since the overall volume fractions were changed of block copolymer segments by 40 hydrogen bonding interactions. Further increasing the OP-POSS contents to approximately 50–80 wt% (higher OP-POSS contents), the self-assembled structures that formed were strongly dependent on the hydrogen bonding strength. For example, the system featuring the strongest hydrogen bonds, the PS-*b*-45 P4VP/OP-POSS complexes, underwent an additional order-order transition to form BCC spheres at an 80 wt% OP-POSS content, with a relatively low value of a_J/a_{J0} (2.35). The PS-*b*-PMMA/OP-POSS complexes, featuring the weakest hydrogen bonds, had already formed a disordered structure at only 50 wt% OP-POSS 50 content. Consistent with this behavior, the PS-*b*-P2VP/OP-POSS hybrid complexes displayed their disordered structure at 60 wt% OP-POSS content.

Conclusions

55 In this study, the phase behavior, hydrogen bonding interaction, and self-assembly structures of PS-*b*-P4VP/OP-POSS, PS-*b*-P2VP/OP-POSS, and PS-*b*-PMMA/OP-POSS complexes were detail investigated by DSC, TEM, SAXS, and FTIR spectroscopy. The self-assembly structure of block copolymer 60 copolymers composites with OP-POSS was strongly dependent on the functional groups polarity of block segments. The relatively weaker intermolecular hydrogen bonding in the PS-*b*-

P2VP/OP-POSS and PS-*b*-PMMA/OP-POSS complexes in block copolymer was formed close-to-disordered structures at relative higher OP-POSS contents. In contrast, the strongest hydrogen bonding interaction in the PS-*b*-P4VP/OP-POSS complexes
[5] induced the order–order transition from alternative lamellae to cylinders and finally to BCC spheres. We conclude that the hydrogen bonding strength, and not the BCP composition, was the key feature affecting the types of self-assembled structures that formed in this study.
[10]

References
[20] 1. Zhang, L.; Li, H.; Wu, L. *Soft Matt.* **2014**, *10*, 6791-6797.
2. Rodriguez-Hernandez, J.; Checot, F.; Gnanou, Y.; Lecommandoux, S. *Prog. Polym. Sci.,* **2005**, *30*, 691-724.
3. Sanchez, C.; Shea, K. J.; Kitagawa, S. *Chem. Soc. Rev.* **2011**, *40*, 471-472.
[25] 4. Pyun, J.; Matyjaszewski, K. *Chem. Mater.* **2001**, *13*, 3436–3448.
5. Zhang, K.; Gao, L.; Chen, Y. *Macromolecules* **2007**, *40*, 5916–5922.
6. Son, J. G.; Hannon, A. F.; Gotrik, K. W.; Alexander-Katz,
[30] A.; Ross, C. A. *Adv. Mater.* **2011**, *23*, 634-639.
7. Borah, D.; Ozmen, M.; Rasappa, S.; Shaw, M. T.; Holmes, J. D.; Morris, M. A. *Langmuir* **2013**, *29*, 2809–2820.
8. Hirai, T.; Leolukman, M.; Jin, S.; Goseki, R.; Ishida, Y.; Kakimoto, M.; Hayakawa, T.; Ree, M.; Gopalan, P.
[35] *Macromolecules* **2009**, *42*, 8835-8843.
9. Hirai, T.; Leolukman, M.; Liu, C. C.; Han, E.; Kim, Y. J.; Ishida, Y.; Hayakawa, T.; Kakimoto, M.; Nealey, P. F.; Gopalan, P. *Adv. Mater.,* **2009**, *21*, 4334-4338.
10. C. W. Chiou, Y. C. Lin, T. Hayakawa, and S. W. Kuo,
[40] *Macromolecules* 2014, 47, 8709-8721.
11. Wu, Y. C.; Kuo, S. W. *J. Mater. Chem.* **2012**, *22,* 2982-2991.
12. Kuo, S. W.; Chang, F. C. *Prog. Polym. Sci.* **2011**, *36*, 1649-1696.
[45] 13. Yu, X.; Yue, K.; Hsieh, I. F.; Li, Y.; Dong, X. H.; Xin, Y.; Wang, H. F.; Shi, A. C.; Newkome, G. R.; Ho, R. M.; Chen, E. Q.; Zhang, W. B.; Cheng, S. Z. D. *Proc. Natl. Acad. Sci.* **2013**, *110,* 10078-10083.
14. Zhang, W. B.; Yu, X.; Wang, C. L.; Sun, H. J.; Hsieh, I. F.;
[50] Li, Y.; Dong, X. H.; Yue, K.; Horn, R. V.; Cheng, S. Z. D. *Macromolecules* **2014**, *47*, 1221–1239.
15. Jang, S. G.; Kramer, E. J.; Hawker, C. J. *J. Am. Chem. Soc.* **2011**, *133,* 16986-16996.
16. Lin, Y.; Daga, V. K.; Anderson, E. R.; Gido, S. P.; Watkins,
[55] J. J. *J. Am. Chem. Soc.* **2011**, *133,* 6513-6516.
17. Daga, V. K.; Anderson, E. R.; Gido S. P.; Watkins, J. J. *Macromolecules* **2011**, *44*, 6793-6799.
18. Noro, A.; Higuchi, K.; Sageshima Y.; Matsushita, Y. *Macromolecules* **2012**, *45*, 8013-8020.
[60] 19. Jang, S. G.; Khan, A.; Hawker, C. J.; Kramer, E. J. *Macromolecules* **2012**, *45,* 1553-1561.
20. Lin, T.; Ho, R. M.; Ho, J. C. *Macromolecules* **2009**, *42,* 742-751.
21. (a) Ramna, V.; Sharma, R.; Hatton, T. A.; Olsen, B. D. *ACS*
[65] *Macro Lett.* **2013**, *2,* 655-659.(b) Zoelen, W.; Vlooswijk, A.

H. G.; Ferri, A.; Andringa, A. M.; Noheda, B.; ten-Brinke, G. *Chem. Mater.* **2009**, *21*, 4719-4723. (c) Thorkelsson, K.; Mastroianni, A. J.; Ercuius, P.; Xu, T. *Nano Lett.* **2012**, *12*, 498-504. (d) Kao, J.; Thorkelsson, K.; Bai, P.; Rancatore, B.
[70] J.; Xu, T. *Chem. Soc. Rev.* **2013**, *42*, 2654-2678.
22. Balazs, A. C.; Emrick, T.; Russell, T. P. *Science* **2006**, *314*, 1107-1110.
23. Cheng, J. Y.; Ross, C. A.; Chan, V. Z. H.; Thomas, E. L.; Lammertink, R. G. H.; Vancso, G. J. *Adv. Mater.* **2001**, *13*,
[75] 1174-1178.
24. Jaramillo, T. F.; Baeck, S. H.; Cuenya, B. R.; McFarland, E. W. *J. Am. Chem. Soc.* **2003**, *125*, 7148-7149.
25. Sarkar, B.; Alexandridis, P. *Langmuir* **2012**, *28*, 15975-15986.
[80] 26. Chiu, J. J.; Kim, B. J.; Kramer, E. J.; Pine, D. J. *J. Am. Chem. Soc.* **2005**, *127*, 5036-5037.
27. Kim, B. J.; Bang, J.; Hawker, C. J.; Kramer, E. J. *Macromolecules* **2006**, *39*, 4108-4114.
28. Park, S. C.; Kim, B. J.; Hawker, C. J.; Kramer, E. J.; Bang,
[85] J.; Ha, J. S. *Macromolecules* **2007**, *40*, 8119-8124.
29. Chiu, J. J.; Kim, B. J.; Yi, G. R.; Bang, J.; Kramer, E. J.; Pine, D. J. *Macromolecules* **2007**, *40*, 3361-3365.
30. Kim, B. J.; Fredrickson, G. H.; Kramer, E. J. *Macromolecules* **2008**, *41*, 436-447.
[90] 31. Hashimoto, T.; Tanaka, H.; Hasegawa, H. *Macromolecules* **1990**, *23*, 4378-4386.
32. Tanaka, T.; Hasegawa, H.; Hashimoto, T. *Macromolecules* **1991**, *24*, 240-251.
33. Jeng, U. S.; Sun, Y. S.; Lee, H. J.; Hsu, C. H.; Liang, K. S.;
[95] Yeh, S. W.; Wei, K. H. *Macromolecules* **2004**, *37*, 4617-4622.
34. Yeh, S. W.; Wei, K. H.; Sun, Y. S.; Jeng, U. S.; Liang, K. S. *Macromolecules* **2003**, *36*, 7903-7907.
35. Yeh, S. W.; Wei, K. H.; Sun, Y. S.; Jeng, U. S.; Liang, K. S.
[100] *Macromolecules* **2005**, *38*, 6559-6565.
36. Lu, C. H.; Kuo, S. W.; Chang, W. T.; Chang, F. C. *Macromol. Rapid Commun.* **2009**, *30*, 2121-2127.
37. Kuo, S. W.; Yang, H. Y. *Macromol. Chem. Phys.* **2011**, *212*, 2249-2259.
[105] 38. Wu, Y. R.; Wu, Y. C.; Kuo, S. W. *Macromol. Chem. Phys.* **2013**, *214*, 1496-1503.
39. Ramanathan, M.; Killbey, S. M.; Ji, Q.; Hill, J. P.; Ariga, K. *J. Mater. Chem.* **2012**, *22*, 10389-10405.
40. Ding, W.; Lin, J.; Yao, K.; Mays, J. W.; Ramanathan, M.;
[110] Hong, K. *J. Mater. Chem. B* **2013**, *1*, 4212-4216.
41. Lu, Y. S.; Kuo, S. W. *RSC Adv.* **2014**, *4*, 34849-34859.
42. Chen, S. C.; Kuo, S. W.; Jeng, U. S.; Su, C. J.; Chang, F. C. *Macromolecules* **2010**, *43*, 1083-1092.
43. Coleman, M. M.; Graf, J. F.; Painter, P. C. "Specific
[115] Interactions and the Miscibility of Polymer Blends. Technomic Publishing", Lancaster, PA, 1991.
44. Lin, C. L.; Chen, W. C.; Liao, C. S.; Su, Y. C.; Huang, C. F.; Kuo, S. W.; Chang, F. C. *Macromolecules* **2005**, *38*, 6435-6444.
[120] 45. Kuo, S. W.; Tung, P. H.; Chang, F. C. *Macromolecules* **2006**, 39, 9388-9395.
46. Sheen, Y. C.; Lu, C. H.; Huang, C. F.; Kuo, S. W.; Chang, F. C. *Polymer* **2008**, *49*, 4017-4024.
47. Yen, Y. J.; Kuo, S. W.; Huang, C. F.; Chen, J. K.; Chang, F.
[125] C. *J. Phys. Chem. B* **2008**, *112*, 10821-10829.
48. Huang, K. W.; Tsai, L. W.; Kuo, S. W. *Polymer* **2009**, *50*, 4876-4887.
49. Kuo, S. W.; Lin, H. C.; Huang, W. J.; Huang, C. F.; Chang, F. C. *J. Polym. Sci.: Polym. Phys.* **2006**, *44,* 673-686.
[130] 50. Kuo, S. W.; Lin, C. L.; Chang, F. C. *Polymer* **2002**, *43*,

3943-3949.

51. Tsitsilianis, C.; Staikos, G. *Macromolecules* **1992**, *25*, 910-916.

52. Kwei, T. K *J. Polym. Sci., Polym. Lett. Ed.* **1984**, *22*, 307-313.

53. Kuo, S. W.; Wu, C. H.; Chang, F. C. *Macromolecules* **2004**, *37*, 192-200.

54. Kuo, S. W. *J. Polym. Res.* **2008**, *15*, 459-486.

55. Huang, C. F.; Kuo, S. W.; Lin, H. C.; Chen, J. K.; Chen, Y. K.; Xu, H. Y.; Chang, F. C. *Polymer* **2004**, *45*, 5913-5921.

56. Huang, C. F.; Kuo, S. W.; Lin, F. J.; Huang, W. J.; Wang, C. F.; Chen, W. Y.; Chang, F. C. *Macromolecules* **2006**, *39*, 300-308.

57. Holoubek, J.; Lednicky, F.; Baldrian, J. *Eur. Polym. J.* **2006**, *42*, 2236-2246.

58. Ruzette, A. V. G.; Mayes, A. M.; Pollard, M.; Russell, T. P.; Hammouda, B. *Macromolecules,* **2003**, *36*, 3351-3356.

59. Wang, J. Y.; Chen, W.; Roy, C.; Sievert, J. D.; Russell, T. P. *Macromolecules* **2008**, *41*, 963-969.

60. Wang, J. Y.; Chen, W.; Russell, T. P. *Macromolecules* **2008**, *41*, 4904-4907.

Graphic Abstract
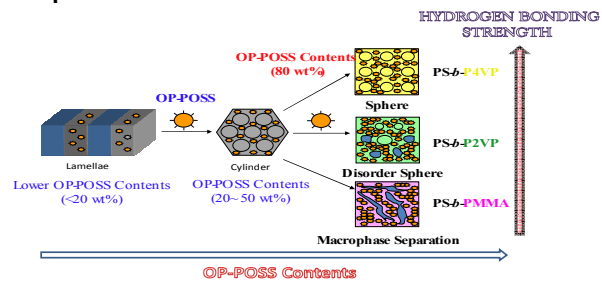
Hydrogen bonding strength on the self-assembled nanostructures formed from block copolymers of PS-*b*-P4VP, PS-*b*-P2VP and PS-*b*-PMMA with OP-POSS nanoparticles.